Imaging electrostatically confined Dirac fermions in graphene quantum dots

Juwon Lee[1†], Dillon Wong[1†], Jairo Velasco Jr[1,2]*, Joaquin F. Rodriguez-Nieva[3], Salman Kahn[1], Hsin-Zon Tsai[1], Takashi Taniguchi[4], Kenji Watanabe[4], Alex Zettl[1,5,6], Feng Wang[1,5,6], Leonid S. Levitov[3] and Michael F. Crommie[1,5,6]*

Electrostatic confinement of charge carriers in graphene is governed by Klein tunnelling, a relativistic quantum process in which particle–hole transmutation leads to unusual anisotropic transmission at p–n junction boundaries[1–5]. Reflection and transmission at these boundaries affect the quantum in-terference of electronic waves, enabling the formation of novel quasi-bound states[6–12]. Here we report the use of scanning tunnelling microscopy to map the electronic structure of Dirac fermions confined in quantum dots defined by circular graphene p–n junctions. The quantum dots were fabricated using a technique involving local manipulation of defect charge within the insulating substrate beneath a graphene monolayer[13]. Inside such graphene quantum dots we observe resonances due to quasi-bound states and directly visualize the quantum interference patterns arising from these states. Outside the quantum dots Dirac fermions exhibit Friedel oscillation-like behaviour. Bolstered by a theoretical model describing relativistic particles in a harmonic oscillator potential, our findings yield insights into the spatial behaviour of electrostatically confined Dirac fermions.

Quantum confinement in graphene has previously been accomplished through lithographically patterned structures[14–17], graphene edges[18], and chemically synthesized graphene islands[19–22]. These systems, however, are either too contaminated for direct wavefunction visualization or use metallic substrates that prevent electrostatic gating. Electron confinement in graphene has also been induced through high magnetic fields[23] and supercritical impurities[24], but these methods are unwieldy for many technological applications. An alternative approach for confining electrons in graphene relies on using electrostatic potentials. However, this is notoriously difficult because Klein tunnelling renders electric potentials transparent to massless Dirac fermions at non-oblique incidence[1–5]. Nevertheless, it has been theoretically predicted that a circular graphene p–n junction can localize Dirac electrons and form quasi-bound quantum dot states[6–11]. A recent tunnelling spectroscopy experiment[12] revealed signatures of electron confinement induced by the electrostatic potential created by a charged scanning tunnelling microscope (STM) tip. However, since the confining potential moves with the STM tip, this method allows neither spatial imaging of the resulting confined modes nor patterning control of the confinement potential.

Here we employ a new patterning technique that allows the creation of stationary circular p–n junctions in a graphene layer on top of hexagonal boron nitride (hBN). Figure 1a illustrates how stationary circular graphene p–n junctions are created. We start with a graphene/hBN heterostructure resting on a SiO_2/Si substrate. The doped Si substrate acts as a global backgate while the hBN layer provides a tunable local embedded gate after being treated by a voltage pulse from an STM tip[13]. To create this embedded gate the STM tip is first retracted approximately 2 nm above the graphene surface and a voltage pulse of $V_s = 5$ V is then applied to the STM tip while simultaneously holding the backgate voltage to $V_g = 40$ V. The voltage pulse ionizes defects in the hBN region directly underneath the tip[25] and the released charge migrates through the hBN to the graphene[13]. This leads to a local space-charge build-up in the hBN that effectively screens the backgate and functions as a negatively charged local embedded gate[13] (using the opposite polarity gate voltage during this process leads to an opposite polarity space charge). Adjusting V_g afterwards allows us to tune the overall doping level so that the graphene is n-doped globally, but p-doped inside a circle centred below the location where the tip pulse occurred (it is also possible to control the charge carrier density profile as well as create opposite polarity p–n junctions by changing the V_g applied during the tip pulse). As shown schematically in Fig. 1b, the STM tip can then be moved to different locations to probe the electronic structure of the resulting stationary circular p–n junction.

To confirm that this procedure results in a circular p–n junction, we measured STM differential conductance (dI/dV_s) as a function of sample bias (V_s) on a grid of points covering the graphene area near a tip pulse. The Dirac point energy, E_D, was identified at every pixel, allowing us to map the charge carrier density, n, through the relation $n(x,y) = -(\text{sgn}(E_D)E_D^2)/(\pi(\hbar v_F)^2)$, where $v_F = 1.1 \times 10^6$ m s^{-1} is the graphene Fermi velocity and $\hbar$ is the reduced Planck constant. Figure 1c shows the resulting $n(x,y)$ for a tip pulse centred in the top right corner (the carrier density n can be adjusted by changing V_g). The interior blue region exhibits positive charge density (p-type) whereas the red region outside has negative charge density (n-type).

To spatially map the local electronic properties of such circular p–n junctions, we examined a rectangular sector near a p–n junction, as indicated in Fig. 2a. Figure 2b shows a topographic image of the clean graphene surface in this region. A 2.8 nm moiré

[1]Department of Physics, University of California, Berkeley, California 94720, USA. [2]Department of Physics, University of California, Santa Cruz, California 95064, USA. [3]Department of Physics, Massachusetts Institute of Technology, 77 Massachusetts Ave, Cambridge, Massachusetts 02139, USA. [4]National Institute for Materials Science, 1-1 Namiki, Tsukuba 305-0044, Japan. [5]Materials Sciences Division, Lawrence Berkeley National Laboratory, Berkeley, California 94720, USA. [6]Kavli Energy NanoSciences Institute at the University of California, Berkeley and the Lawrence Berkeley National Laboratory, Berkeley, California 94720, USA. [†]These authors contributed equally to this work. *e-mail: jvelasc5@ucsc.edu; crommie@berkeley.edu

pattern (corresponding to a 5° rotation angle between graphene and hBN) is visible[26,27] and the region is seen to be free of adsorbates. A dI/dV_s map of the same region (Fig. 2c) reflects changes in the local density of states (LDOS) caused by the spatially varying charge density distribution. Since the p–n junction centre is stationary, we are able to move the STM tip to different locations inside and outside the p–n junction to spatially resolve the resulting electronic states. Figure 2d–g shows $d^2I/dV_s^2(V_g, V_s)$ plots at four different locations, as denoted in Fig. 2c. We plot the derivative of dI/dV_s with respect to V_s to accentuate the most salient features, which are quasi-periodic resonances that disperse to lower energies with increasing V_g (see Supplementary Section 2 for dI/dV_s sweeps before differentiation). The energies of the observed resonances are seen to evolve as $\varepsilon \propto \sqrt{|V_g - V_{CNP}|} + \text{constant}$, where V_{CNP} is the local charge neutrality point, as expected for graphene's relativistic band structure. We see that the energy spacing between observed resonances ($\Delta\varepsilon$) decreases as we move away from the p–n junction centre until the resonances disappear outside. For example, $\Delta\varepsilon$ is 29 ± 2 mV at the centre, 16 ± 2 mV at 50 nm from the centre, and 13 ± 2 mV at 100 nm from the centre (for $V_g = 32$ V). A similar trend is also observed for p–n junctions that are n-doped in the centre and p-doped outside (Supplementary Section 3).

We have imaged these electronic states both inside and outside of circular p–n junctions. The dI/dV_s maps in Fig. 3a,b show eigenstate distributions mapped at two different energies within the same section of a circular p–n junction (similar to the boxed region of Fig. 2a, but with opposite heterojunction polarity). Circular quantum interference patterns resulting from confined Dirac fermions are clearly observed within the junction boundary, as well as scattering states exterior to the boundary. The junction boundary is demarcated by a dark band (low dI/dV_s) in the middle of each dI/dV_s map (and further marked by a dashed line). Comparing the overall spatial locations of the nodes and anti-nodes, the two eigenstate distributions in Fig. 3a,b are clearly different (for example, one has a node at the origin, whereas the other exhibits a central anti-node). Figure 4a shows a more complete mapping of the energy-dependent eigenstates (within a p–n junction of the same polarity as Fig. 2a) along a line extending from the centre (left edge) to a point outside of the p–n junction (right edge) at a gate voltage of $V_g = 32$ V. The data are plotted as $d^2I/dV_s^2(r, V_s)$ (where r is the radial distance from the centre) to accentuate the striking oscillatory features (see Supplementary Section 2 for $dI/dV_s(r, V_s)$ before differentiation). The energy level structure and interior nodal patterns are clearly evident.

Our observations can be explained by considering the behaviour of massless Dirac fermions in response to a circular electrostatic potential. Due to Klein tunnelling, a graphene p–n junction perfectly transmits quasiparticles at normal incidence to the boundary, but reflects them at larger angles of incidence[1,4,5]. In a potential well with circular symmetry, electrons with high angular momenta are obliquely incident on the barrier and are internally reflected, thus leading to particle confinement and the formation of quasi-bound quantum dot states[7–12]. As angular momentum is increased, electrons are repelled from the centre of the potential by the centrifugal barrier, leading to an increase in the number of dI/dV_s resonances that should be observable in spectroscopy measured away from the centre[28]. This is consistent with our observation that the apparent energy spacing between resonances ($\Delta\varepsilon$) at the centre (Fig. 2d) is approximately double the apparent energy spacing at a point 100 nm away from the centre (Fig. 2f). Scattered quasiparticles (with nonzero angular momenta) external to the potential boundary contribute to Friedel oscillations that radiate outwards, as seen in Fig. 3. A circular graphene p–n junction with an n-doped interior thus acts as a quantum dot for electron-like carriers and a quantum antidot for hole-like carriers (as in Fig. 3), whereas the reverse is true for p–n junctions of opposite polarity (as in Figs 2 and 4).
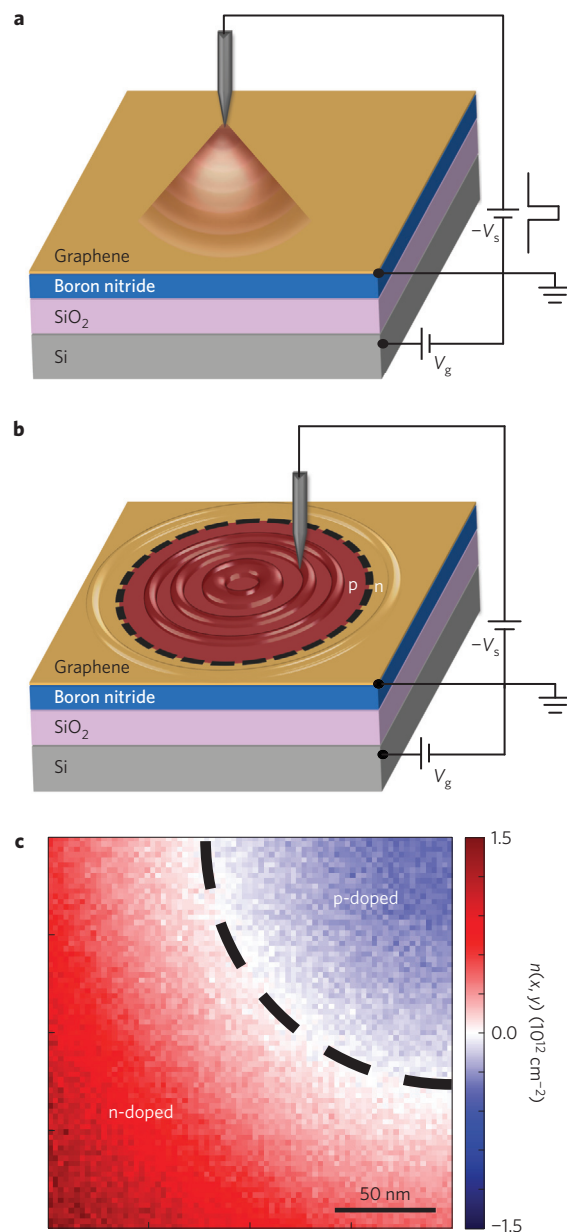
Figure 1 | Creating and imaging a circular graphene p–n junction.
a, Schematic diagram showing the fabrication of a local embedded gate in a graphene/hBN heterostructure. A square voltage pulse is applied to the STM tip (held a few nanometres from the graphene surface) while the backgate voltage V_g is fixed at a nonzero value. V_s is defined as the negative of the tip bias. This technique creates a circular p–n junction in the graphene in response to trapped space charge in the insulating hBN. **b**, The STM tip spatially probes Dirac fermion wavefunctions in the presence of the p–n junction. **c**, A representative experimental charge density map for one quadrant of a circular graphene p–n junction. A dI/dV_s spectrum is measured at each pixel to determine the Dirac point energy $E_D(x,y)$, which is then converted to a local charge carrier density $n(x,y)$. The black dashed line marks the approximate location of the p–n junction boundary at $V_g = 40$ V.

This qualitative picture can be confirmed by comparing the experimental results to a model based on the two-dimensional massless Dirac Hamiltonian, $H = -i\hbar v_F \boldsymbol{\sigma} \cdot \nabla_r + U(\boldsymbol{r})$, where $U(\boldsymbol{r})$ is a scalar potential and $\boldsymbol{\sigma} = (\sigma_x, \sigma_y)$ are the pseudospin Pauli matrices. Since we are interested in the low-energy eigenstates of the confinement potential, we use a parabolic model $U(r) = -\kappa r^2$ (that
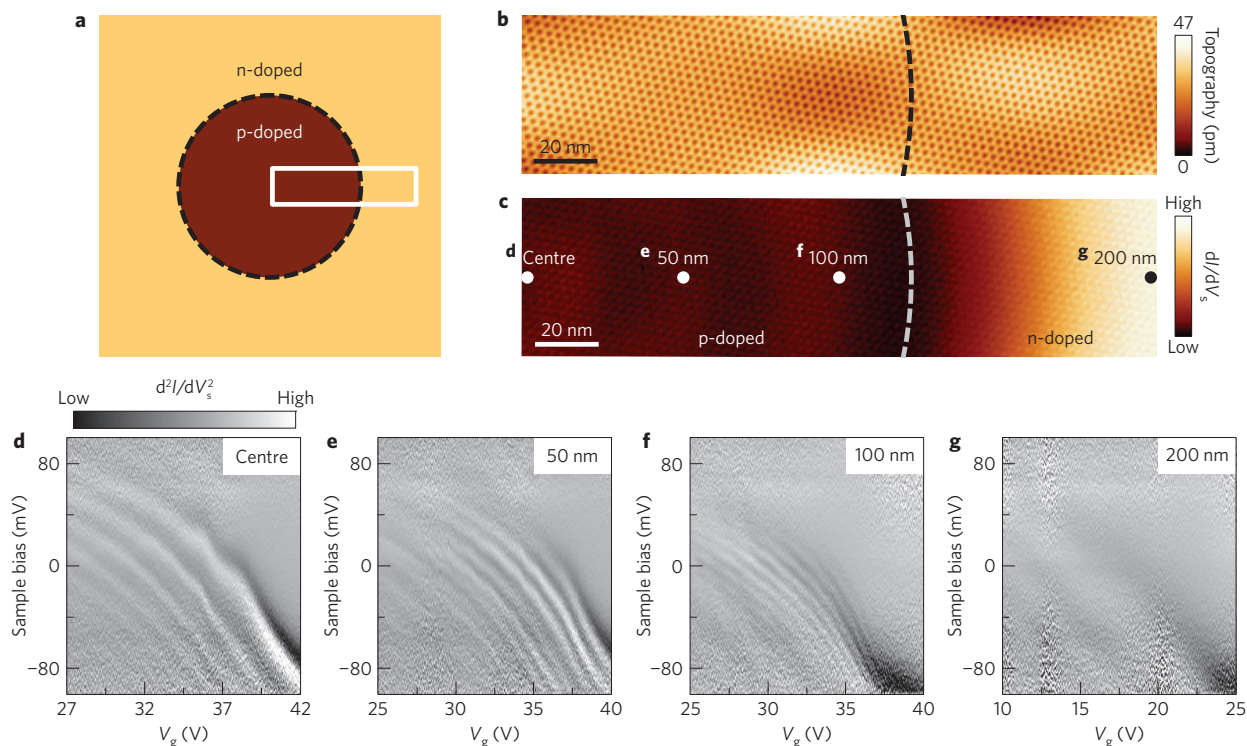
Figure 2 | Gate-tunable electronic structure of a circular graphene p–n junction. a, Schematic diagram of a circular p–n junction formed in graphene. The white rectangle indicates the measurement region. **b**, STM topographic image of the region sketched in **a**. **c**, dI/dV_s map of the same region as shown in **b**. Dashed lines are placed near the p–n junction boundary in **b** and **c** to serve as guides to the eye. ($V_s = -0.25$ V, $I = 0.5$ nA, $V_g = 30$ V, 6 mV root-mean squared a.c. modulation added to V_s.) **d–g**, $d^2I/dV_s^2(V_g, V_s)$ plots measured at different distances from the centre, as indicated in **c** (initial tunnelling parameters: $V_s = -0.1$ V, $I = 1.5$ nA, 1 mV a.c. modulation). The grey scale bar in **d** also applies to **e–g**. The observed resonances vary in energy roughly according to the expected graphene dispersion $\varepsilon \propto \sqrt{|V_g - V_{CNP}|}$. The energy spacing between resonances is larger at the centre (**d**) than is seen further out (**e**,**f**), and the resonances disappear altogether beyond the p–n junction boundary (**g**).
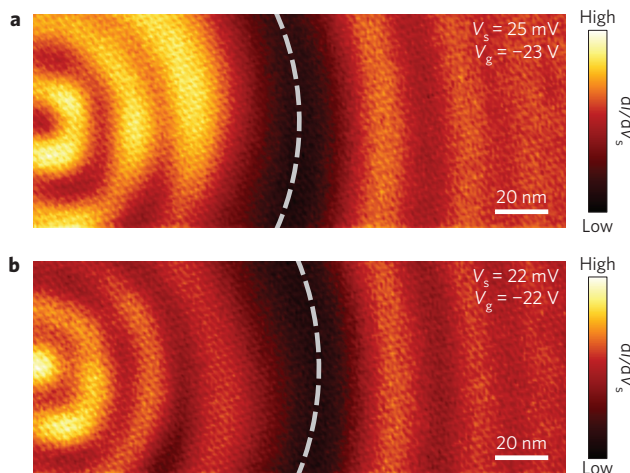

Figure 3 | dI/dV_s images of quantum interference throughout a circular graphene p–n junction. a, dI/dV_s map measured for a p–n junction sector similar to Fig. 2a, but having opposite heterojunction polarity ($V_s = 25$ mV, $I = 0.5$ nA, $V_g = -23$ V, 1 mV a.c. modulation). **b**, dI/dV_s map at the same location as **a**, but for a different energy, shows a different spatial pattern ($V_s = 22$ mV, $I = 0.4$ nA, $V_g = -22$ V, 1 mV a.c. modulation). The dark bands (low dI/dV_s) marked by the dashed lines in the middle of **a** and **b** represent the classical turning points of the potential.

is, the lowest order approximation). The curvature of the potential, $\kappa = 6 \times 10^{-3}$ meV nm^{-2}, was extracted from measurements of the spatially dependent Dirac point energy (Supplementary Section 1).

We solved the Dirac equation to obtain the eigenstates for Dirac fermions in this confinement potential (see Methods).

Figure 4b shows the results of our calculations in a plot of ∂LDOS$/\partial\varepsilon$, the energy derivative of the LDOS, which corresponds to the experimental quantity d^2I/dV_s^2. The resulting eigenstate distribution (Fig. 4b) closely resembles the experimental eigenstate distribution (Fig. 4a). Both have a characteristic parabolic envelope due to the confinement potential, as well as a complex set of interior nodal patterns. The characteristic energy spacing seen experimentally is in good agreement with the characteristic energy scale $\varepsilon^* = (\hbar^2 v_F^2 \kappa)^{1/3} \approx 15$ meV that arises from the theoretical model.

Further insight into the nature of the observed resonances can be gained by directly comparing constant-energy experimental dI/dV_s line-cuts (Fig. 4c) to the modulus square of the simulated quantum dot wavefunctions (Fig. 4d). Here it is useful to label the confined states by a radial quantum number $n = 0, 1, 2, \ldots$ and an azimuthal quantum number $m = \pm(1/2), \pm(3/2), \ldots$, that is, $H\Psi_{n,m} = \varepsilon_{n,m}\Psi_{n,m}$. To understand the experimentally observed behaviour, we note two important properties of the eigenstates $\Psi_{n,m}$. First, although each probability distribution $|\Psi_{n,m}|^2$ features $n + 1$ maxima, most of the weight is concentrated in the first maximum. The position of this maximum is pushed further from the centre for larger values of $|m|$ (Fig. 4d). Second, for massless Dirac fermions confined by a quadratic potential, we observe a near-perfect energy alignment of the states $\varepsilon_{n,m}, \varepsilon_{n-1,m+2}, \ldots$ at low quantum numbers, indicating an approximate degeneracy. This degeneracy explains why different resonances originating from different $\Psi_{n,m}$ states form the horizontal rows seen in Fig. 4a,b (which are not perfectly horizontal because the degeneracy is not perfect). Combining these two observations,
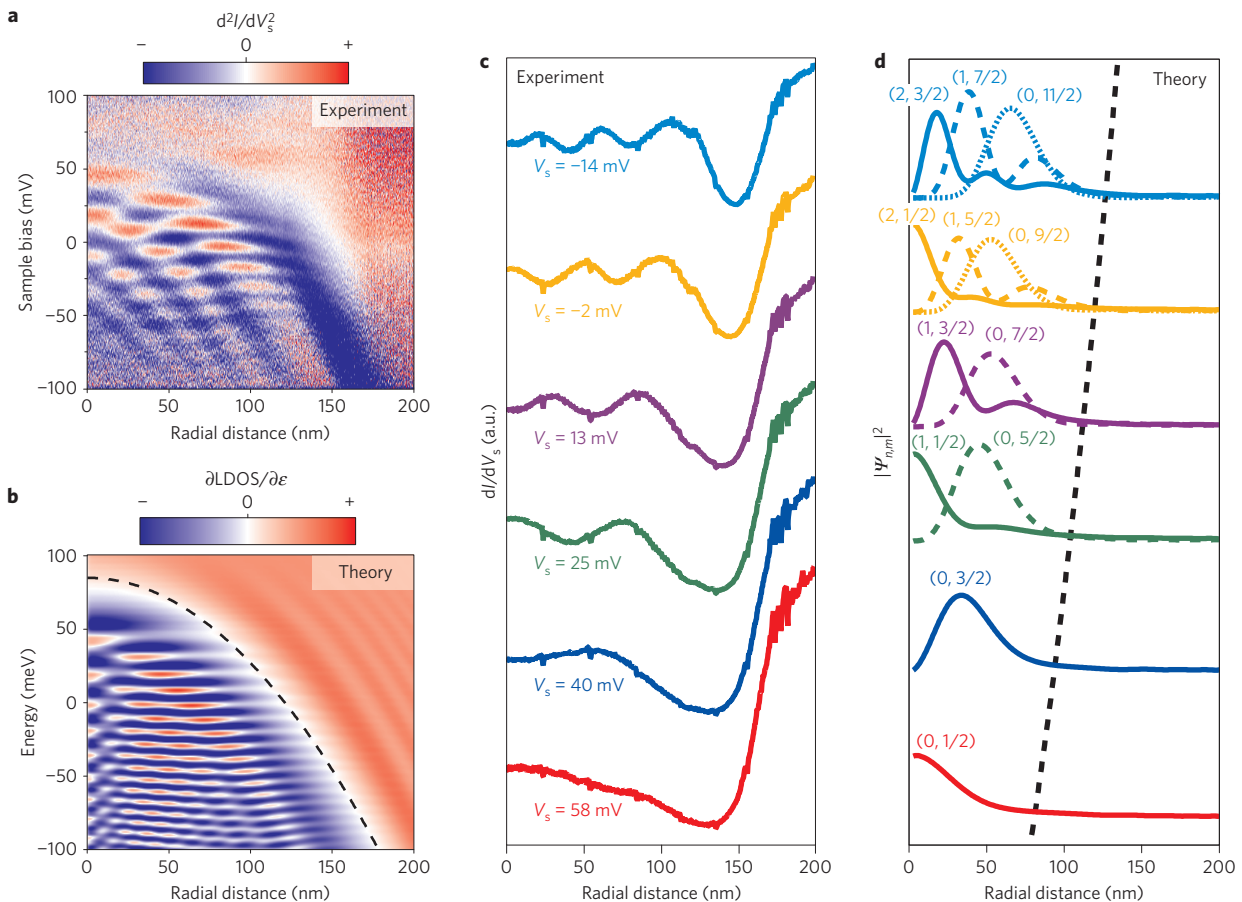
Figure 4 | Spatially resolving energy levels inside a circular graphene p–n junction. a, d^2I/dV_s^2 measured as a function of V_s and the radial distance r from the centre of a circular p–n junction having the same polarity as Fig. 2a. The measurement was performed at a fixed gate voltage (initial tunnelling parameters: $V_g = 32$ V, $V_s = -0.1$ V, $I = 1.5$ nA, 1 mV a.c. modulation). **b**, Theoretically simulated $\partial LDOS/\partial \varepsilon$ as a function of energy and radial distance for a potential $U(\mathbf{r}) = -\kappa r^2$ (potential shown as dashed line). **c**, Experimental dI/dV_s radial line scans at different V_s values for fixed $V_g = 32$ V. **d**, Radial dependence of the theoretical probability density $|\Psi_{n,m}|^2$ for quantum dot eigenstates. Each curve is labelled by radial and azimuthal quantum numbers (n, m). Each set of theoretical curves has been vertically displaced by a quantity proportional to V_s for the correspondingly coloured experimental curve in **c** to ensure that the black dashed line denotes the classical turning points.

we are able to attribute each experimental dI/dV_s peak in Fig. 4c to a different $\Psi_{n,m}$ state, wherein each eigenstate contributes most of its spectral weight to a single energy and radial position.

In addition to providing insight into the spatial and spectral distribution of the $\Psi_{n,m}$ states, our simulations also explain other key aspects of the experimental data. In particular, the resonances in our simulation have finite widths, originating from Klein tunnelling of confined states into the Dirac continuum. The widths of these resonances lie within the range 4 meV to 10 meV for both the experimental data and the theoretical simulation (Supplementary Section 6). Furthermore, our simulation also explains the striking observation that the apparent energy spacing for the resonances close to the centre is nearly twice as large as the spacing away from the centre (see Fig. 2d). This occurs because only the lowest angular momentum states, $m = \pm 1/2$, have appreciable wavefunction density at the origin, whereas for all other m values the $\Psi_{n,m}$ states contribute predominantly to off-centred measurements.

In conclusion, we have spatially mapped the electronic structure inside and outside of highly tunable quantum dots formed by circular graphene p–n junctions. In contrast to conventional semiconductor quantum dots, these new graphene quantum dots are fully exposed and directly accessible to real-space imaging tools. The techniques presented here might be extended to more complicated systems such as multiple quantum dots[29,30] with variable coupling and arbitrary geometries.

Note added in proof: After acceptance of this paper, we became aware of a related manuscript (ref. 31) showing similar results to this work.

Methods

Methods, including statements of data availability and any associated accession codes and references, are available in the online version of this paper.

References

1. Katsnelson, M. I., Novoselov, K. S. & Geim, A. K. Chiral tunnelling and the Klein paradox in graphene. *Nature Phys.* **2**, 620–625 (2006).
2. Young, A. F. & Kim, P. Quantum interference and Klein tunnelling in graphene heterojunctions. *Nature Phys.* **5**, 222–226 (2009).
3. Stander, N., Huard, B. & Goldhaber-Gordon, D. Evidence for Klein tunneling in graphene p-n junctions. *Phys. Rev. Lett.* **102**, 026807 (2009).
4. Cheianov, V. V. & Fal'ko, V. I. Selective transmission of Dirac electrons and ballistic magnetoresistance of n-p junctions in graphene. *Phys. Rev. B* **74**, 041403 (2006).
5. Shytov, A. V., Rudner, M. S. & Levitov, L. S. Klein backscattering and Fabry–Pérot interference in graphene heterojunctions. *Phys. Rev. Lett.* **101**, 156804 (2008).
6. Downing, C. A., Stone, D. A. & Portnoi, M. E. Zero-energy states in graphene quantum dots and rings. *Phys. Rev. B* **84**, 155437 (2011).

7. Wu, J.-S. & Fogler, M. M. Scattering of two-dimensional massless Dirac electrons by a circular potential barrier. *Phys. Rev. B* **90,** 235402 (2014).
8. Schulz, C., Heinisch, R. L. & Fehske, H. Scattering of two-dimensional Dirac fermions on gate-defined oscillating quantum dots. *Phys. Rev. B* **91,** 045130 (2015).
9. Chen, H.-Y., Apalkov, V. & Chakraborty, T. Fock–Darwin states of Dirac electrons in graphene-based artificial atoms. *Phys. Rev. Lett.* **98,** 186803 (2007).
10. Matulis, A. & Peeters, F. M. Quasibound states of quantum dots in single and bilayer graphene. *Phys. Rev. B* **77,** 115423 (2008).
11. Bardarson, J. H., Titov, M. & Brouwer, P. W. Electrostatic confinement of electrons in an integrable graphene quantum dot. *Phys. Rev. Lett.* **102,** 226803 (2009).
12. Zhao, Y. *et al*. Creating and probing electron whispering-gallery modes in graphene. *Science* **348,** 672–675 (2015).
13. Velasco, J. Jr *et al*. Nanoscale control of rewriteable doping patterns in pristine graphene/boron nitride heterostructures. *Nano Lett.* **16,** 1620–1625 (2016).
14. Ponomarenko, L. A. *et al*. Chaotic Dirac Billiard in graphene quantum dots. *Science* **320,** 356–358 (2008).
15. Schnez, S. *et al*. Imaging localized states in graphene nanostructures. *Phys. Rev. B* **82,** 165445 (2010).
16. Todd, K., Chou, H.-T., Amasha, S. & Goldhaber-Gordon, D. Quantum dot behavior in graphene nanoconstrictions. *Nano Lett.* **9,** 416–421 (2009).
17. Han, M. Y., Özyilmaz, B., Zhang, Y. & Kim, P. Energy band-gap engineering of graphene nanoribbons. *Phys. Rev. Lett.* **98,** 206805 (2007).
18. Allen, M. T. *et al*. Spatially resolved edge currents and guided-wave electronic states in graphene. *Nature Phys.* **12,** 128–133 (2016).
19. Subramaniam, D. *et al*. Wave-Function mapping of graphene quantum dots with soft confinement. *Phys. Rev. Lett.* **108,** 046801 (2012).
20. Hämäläinen, S. K. *et al*. Quantum-confined electronic states in atomically well-defined graphene nanostructures. *Phys. Rev. Lett.* **107,** 236803 (2011).
21. Phark, S.-h. *et al*. Direct observation of electron confinement in epitaxial graphene nanoislands. *ACS Nano* **5,** 8162–8166 (2011).
22. Lu, J., Yeo, P. S. E., Gan, C. K., Wu, P. & Loh, K. P. Transforming C_{60} molecules into graphene quantum dots. *Nature Nanotech.* **6,** 247–252 (2011).
23. Jung, S. *et al*. Evolution of microscopic localization in graphene in a magnetic field from scattering resonances to quantum dots. *Nature Phys.* **7,** 245–251 (2011).
24. Wang, Y. *et al*. Observing atomic collapse resonances in artificial nuclei on graphene. *Science* **340,** 734–737 (2013).
25. Wong, D. *et al*. Characterization and manipulation of individual defects in insulating hexagonal boron nitride using scanning tunnelling microscopy. *Nature Nanotech.* **10,** 949–953 (2015).
26. Xue, J. *et al*. Scanning tunnelling microscopy and spectroscopy of ultra-flat graphene on hexagonal boron nitride. *Nature Mater.* **10,** 282–285 (2011).
27. Decker, R. *et al*. Local electronic properties of graphene on a BN substrate via scanning tunneling microscopy. *Nano Lett.* **11,** 2291–2295 (2011).
28. Crommie, M. F., Lutz, C. P. & Eigler, D. M. Confinement of electrons to quantum corrals on a metal surface. *Science* **262,** 218–220 (1993).
29. Laird, E. A. *et al*. Quantum transport in carbon nanotubes. *Rev. Mod. Phys.* **87,** 703–764 (2015).
30. van der Wiel, W. G. *et al*. Electron transport through double quantum dots. *Rev. Mod. Phys.* **75,** 1–22 (2002).
31. Gutiérrez, C., Brown, L., Kim, C.-J., Park, J. & Pasupathy, A. N. Klein tunnelling and electron trapping in nanometre-scale graphene quantum dots. *Nature Phys.* http://dx.doi.org/10.1038/nphys3806 (2016).

Author contributions

J.V.Jr, D.W. and J.L. conceived the work and designed the research strategy. D.W., J.L., J.F.R.-N. and J.V.Jr performed data analysis. S.K., J.V.Jr and A.Z. facilitated sample fabrication. J.L., D.W. and J.V.Jr carried out STM/STS measurements. K.W. and T.T. synthesized the hBN samples. J.F.R.-N. and L.S.L. performed theoretical calculations. M.F.C. supervised the STM/STS experiments. J.L., D.W., J.V.Jr, J.F.R.-N., L.S.L. and M.F.C. co-wrote the manuscript. D.W. and M.F.C. coordinated the collaboration. All authors discussed the results and commented on the paper.

Additional information

Supplementary information is available in the online version of the paper. Reprints and permissions information is available online at www.nature.com/reprints. Correspondence and requests for materials should be addressed to J.V.Jr or M.F.C.

Competing financial interests

The authors declare no competing financial interests.

Methods

Sample fabrication. We fabricated our samples using a transfer technique[32] that uses 60–100-nm-thick hexagonal boron nitride (hBN) crystals (synthesized by Taniguchi and Watanabe[33]) and 300-nm-thick SiO$_2$ as the dielectric for electrostatic gating. Single-layer graphene was mechanically exfoliated from graphite and deposited onto methyl methacrylate (MMA) before being transferred onto hBN previously exfoliated onto a heavily doped SiO$_2$/Si wafer. The graphene was electrically grounded through a Ti (10 nm)/Au (100 nm) electrode deposited via electron beam evaporation using a shadow mask. Devices were annealed in Ar/H$_2$ gas at 350 °C before being transferred into our Omicron ultrahigh vacuum (UHV) low-temperature scanning tunnelling microscope (STM). A second anneal was performed overnight at 250–400 °C and 10^{-11} torr.

STM and spectroscopy measurements. STM measurements were performed at $T = 4.8$ K with a platinum iridium STM tip calibrated against the Au(111) Shockley surface state. STM topographic and dI/dV_s images were obtained at constant current with sample bias V_s, defined as the negative of the voltage applied to the STM tip with respect to the grounded graphene sample. A voltage V_g is applied to Si to electrostatically gate graphene. Scanning tunnelling spectroscopy (STS) measurements were performed by lock-in detection of the a.c. tunnel current induced by a modulated voltage (1–6 mV at 613.7 Hz) added to V_s, while dI/d$V_s(V_g, V_s)$ and dI/d$V_s(r, V_s)$ measurements were acquired by sweeping V_s (starting from a fixed set of initial tunnelling parameters) and then incrementing V_g for dI/d$V_s(V_g, V_s)$ and r for dI/d$V_s(r, V_s)$. Measurements were restricted to -0.1 eV $< V_s < 0.1$ eV to avoid energy broadening induced by phonon-assisted inelastic tunnelling[34]. All d^2I/dV_s^2 figures are numerical derivatives of dI/dV_s with respect to V_s. These results were reproduced with numerous STM tips on more than 30 p–n junction structures.

Creation of graphene p–n junction. The STM tunnelling bias and current are set to $V_s = -0.5$ V and $I = 0.5$ nA, respectively. To create a circular graphene p–n junction that is p-doped (n-doped) at the centre, we set $V_g = 40$ V ($V_g = -40$ V). The STM feedback loop is opened, and the STM tip is withdrawn by $\Delta z \sim 1.5$–2 nm. The sample bias is increased to $V_s = 5$ V for 1 min. The sample bias is then decreased to $V_s = -0.5$ V.

Theoretical modelling. The eigenstates of the Dirac equation are obtained by solving $[v_F \boldsymbol{\sigma} \cdot \boldsymbol{p} + U(\boldsymbol{r})]\Psi(\boldsymbol{r}) = \varepsilon \Psi(\boldsymbol{r})$, where $U(\boldsymbol{r})$ is the electrostatic potential and $\boldsymbol{p} = -i\hbar\nabla_r$. Because $U(\boldsymbol{r})$ is radially symmetric, we use the polar decomposition ansatz

$$\Psi_m(r, \theta) = \frac{e^{im\theta}}{\sqrt{r}} \begin{pmatrix} u_1(r) e^{-i\theta/2} \\ i u_2(r) e^{i\theta/2} \end{pmatrix}$$

where m is a half-integer. By inserting the ansatz into the eigenvalue equation we obtain

$$\begin{pmatrix} [U(r) - \varepsilon]/\hbar v_F & \partial_r + m/r \\ -\partial_r + m/r & [U(r) - \varepsilon]/\hbar v_F \end{pmatrix} u(r) = 0$$

To make direct connection with the STS measurements we calculate the local density of states LDOS(ε) as a function of r. The LDOS can be written as the sum of m-state contributions, LDOS$(\varepsilon) = \sum_m$ LDOS$_m(\varepsilon)$, with

$$\text{LDOS}_m(\varepsilon) = \sum_\nu \langle |u_\nu(r)|^2 \rangle_\lambda \delta(\varepsilon - \varepsilon_\nu)$$

where ν labels the radial eigenstates for fixed m and $\langle |u_\nu(r)|^2 \rangle_\lambda = \int_0^\infty \mathrm{d}r' |u_\nu(r')|^2 e^{-(r-r')^2/2\lambda}$ represents a spatial average of the wavefunction centred at r with a Gaussian weight $\lambda/r^* = 0.01$. To solve the radial Dirac equation, we use the finite difference method discretized in 1,200 lattice sites in the interval $0 < r < L$, with a large repulsive potential at $r = L = 12r^*$. Spurious states arising from the finite potential jumps at the boundaries, localized within a few lattice sites of $r = 0$ and $r = L$, are excluded. We sum over eigenstates with azimuthal quantum numbers $-401/2 \leq m \leq 401/2$, which is sufficient to accurately represent the states in the energy range of interest. The delta function is approximated as a Lorentzian with width $0.3\varepsilon^*$, which is sufficiently small that the intrinsic linewidths of the quantum dot eigenstates are preserved.

Data availability. The data that support the plots within this paper and other findings of this study are available from the corresponding author on reasonable request.

References

32. Zomer, P. J., Dash, S. P., Tombros, N. & van Wees, B. J. A transfer technique for high mobility graphene devices on commercially available hexagonal boron nitride. *Appl. Phys. Lett.* **99,** 232104–232107 (2011).
33. Watanabe, K., Taniguchi, T. & Kanda, H. Direct-bandgap properties and evidence for ultraviolet lasing of hexagonal boron nitride single crystal. *Nature Mater.* **3,** 404–409 (2004).
34. Brar, V. W. *et al*. Observation of carrier-density-dependent many-body effects in graphene via tunneling spectroscopy. *Phys. Rev. Lett.* **104,** 036805 (2010).